Research Article

Carrier-free cryptotanshinone-peptide conjugates self-assembled nanoparticles: An efficient and low-risk strategy for acne vulgaris

Quanfu Zeng [a,b,1], Hongkai Chen [b,1], Zhuxian Wang [a,1], Yinglin Guo [b,1], Yufan Wu [b], Yi Hu [b], Peiyi Liang [b], Zeying Zheng [b], Tao Liang [b], Dan Zhai [b], Yaling Guo [b], Li Liu [b], Chunyan Shen [b], Cuiping Jiang [b], Qun Shen [b], Yankui Yi [b], Qiang Liu [a,*]

[a] Dermatology Hospital, Southern Medical University, Guangzhou 510091, China
[b] School of Traditional Chinese Medicine, Southern Medical University, Guangzhou 510515, China

ABSTRACT

Acne vulgaris ranks as the second most prevalent dermatological condition worldwide, and there are still insufficient safe and reliable drugs to treat it. Cryptotanshinone (CTS), a bioactive compound derived from traditional Chinese medicine *Salvia miltiorrhiza*, has shown promise for treating acne vulgaris due to its broad-spectrum antimicrobial and significant anti-inflammatory properties. Nevertheless, its local application is hindered by its low solubility and poor skin permeability. To overcome these challenges, a carrier-free pure drug self-assembled nanosystem is employed, which can specifically modify drug molecules based on the disease type and microenvironment, offering a potential for more effective treatment. We designed and synthesized three distinct structures of cationic CTS-peptide conjugates, creating self-assembled nanoparticles. This study has explored their self-assembly behavior, skin permeation, cellular uptake, and both *in vitro* and *in vivo* anti-acne effects. Molecular dynamics simulations revealed these nanoparticles form through intermolecular hydrogen bonding and π-π stacking interactions. Notably, self-assembled nanoparticles demonstrated enhanced bioavailability with higher skin permeation and cellular uptake rates. Furthermore, the nanoparticles exhibited superior anti-acne effects compared to the parent drug, attributed to heightened antimicrobial activity and significant downregulation of the MAPK/NF-κB pathway, leading to reduced expression of pro-inflammatory factors including TNF-α, IL-1β and IL-8. In summary, the carrier-free self-assembled nanoparticles based on CTS-peptide conjugate effectively address the issue of poor skin bioavailability, offering a promising new approach for acne treatment.

* Corresponding author.
  E-mail address: liuqiang@smu.edu.cn (Q. Liu).
[1] These authors contributed equally to this work.
  Peer review under responsibility of Shenyang Pharmaceutical University.

1. Introduction

Acne vulgaris, commonly referred to as acne, represents a chronic inflammatory skin disorder involving the pilosebaceous unit, impacting an estimated 650 million individuals globally. This condition predominantly emerges on the facial, chest, upper back, and neck regions, exerting significant influences on both the quality of life and psychological well-being of patients, particularly among adolescents and professional women [1,2]. Prior investigations have definitively identified the colonization of *Propionibacterium acnes* (*P. acnes*), excessive sebum secretion, follicular hyperkeratinization, and the ensuing inflammation as primary instigators of acne development [3-5]. Moreover, the excessive production of androgens has been established as a contributing factor in the initiation of this condition [6]. Current research underscores the enzymatic hydrolysis of sebum into liberated fatty acids by *P. acnes*, a bacterium closely associated with acne, facilitated by its own lipase secretion. These liberated fatty acids, once released, stimulate the follicular epithelium, inciting an inflammatory cascade [7]. The coexistence of lipases and the acidic milieu characteristic of acne presents a strategic opportunity for the targeted release of therapeutic agents, specifically at sites of *P. acnes* infection and resultant inflammation [4,8].

Currently, the clinical management of acne heavily relies on the utilization of anti-inflammatory and antimicrobial medications. However, the direct application of most of these agents proves insufficient in comprehensively addressing all underlying factors, potentially leading to the activation of adverse reactions such as allergies and skin irritation [9-11]. Consequently, the development of innovative, secure, and efficacious anti-acne formulations is of paramount importance. When compared to synthetic pharmaceuticals, active compounds derived from medicinal plants for acne treatment offer distinctive benefits, including heightened biocompatibility and limited adverse effects [12,13].

Within this context, tanshinone emerges as a class of pivotal lipophilic derivatives extracted from *Salvia miltiorrhiza* Bunge, a well-known traditional Chinese herbal. Tanshinone belongs to the class of diterpene quinone compounds, frequently characterized by tricyclic or tetracyclic benzoquinone or naphthoquinone configurations, which often confer antioxidant, anti-inflammatory, and antibacterial attributes [5,14,15]. Remarkably, cryptotanshinone (CTS) stands out as the most potent antibacterial monomer within tanshinone, displaying substantial inhibitory effects against diverse Gram-positive bacteria, including *Staphylococcus aureus* (Sau.), *Staphylococcus epidermidis* (Sep.) and *P. acnes* [5,16]. Recent investigations propose that CTS may function as a respiratory chain inhibitor, specifically targeting microbial cell membranes. CTS accomplishes this by depleting intrabacterial oxygen, primarily by targeting both type I and type II NADH dehydrogenases, consequently resulting in the inhibition of bacterial proliferation [17]. Additionally, the generation of superoxide radicals induced by CTS is speculated to significantly contribute to its antibacterial effects, albeit the precise mechanism remains unclear. Furthermore, the acne treatment mechanism of CTS correlates with its anti-inflammatory and anti-androgen pharmacological activities [5]. Thus, CTS exhibits the potential to serve as an innovative anti-acne agent capable of combating multidrug-resistant microbial strains. Nevertheless, addressing the challenge of CTS's limited bioavailability due to its low solubility and inadequate cutaneous penetration upon localized application is an essential prerequisite [10,18]. In this study, we contemplate performing structural modifications on CTS to enhance its aqueous solubility and cutaneous permeability and constructing carrier-free pure drug self-assembled nanosystems. This approach aims to overcome the limitations of local skin administration of CTS and improve its local bioavailability.

Carrier-free pure drug self-assembled nanosystems have surfaced as an exceptionally auspicious integrated therapeutic approach owing to their ecologically sound and uncomplicated manufacturing process, substantial drug-loading capability, amplified pharmacological impacts, absence of non-therapeutic adjuncts, and negligible adverse effects [19-21]. The preponderance of drug molecules encapsulated in these systems inherently exhibit amphiphilic traits, encompassing hydrophilic and hydrophobic domains. This pivotal attribute inherently facilitates their innate self-assembly in aqueous surroundings. Beyond the advantages of accommodating larger quantities of drugs and reducing the potential for long-term or short-term toxicity associated with the use of carrier materials, carrier-free pure drug self-assembled nanosystems can be precisely tailored according to specific routes of administration and disease treatments. For instance, the membrane permeability of hydrophilic drugs can be enhanced through ester bond formation [22]; the solubility of hydrophobic drugs can be augmented by introducing ionizable groups [23]; or selective release at disease sites can be achieved through the integration of ligands sensitive to binding [24]. In terms of self-assembly, carrier-free pure drugs provide an expansive spatial realm for generating supramolecular structures. Nonetheless, their comparatively smaller molecular dimensions signify that any binding groups can readily exert distinct effects on the arrangement of molecular space and interactions between molecules. Consequently, the choice of connecting compounds assumes utmost importance.

Antimicrobial peptides (AMPs) are short oligopeptides of varying lengths that are produced by plants, animals, and microorganisms [25]. In recent years, there has been a growing focus on the application of natural or synthetic AMPs for addressing skin wound infections and common acne. This heightened interest can be attributed to the fact that, when compared to antibiotics, AMPs present distinct advantages, including a wider antimicrobial spectrum and reduced likelihood of resistance development [26,27]. AMPs commonly manifest properties such as cationic, hydrophobic, or amphiphilic characteristics. Remarkably, their mechanism of action against microbes involves an electrostatic interaction between positively charged amino acids or guanidine moieties, carrying an overall positive charge within the peptide chain, and the phospholipids
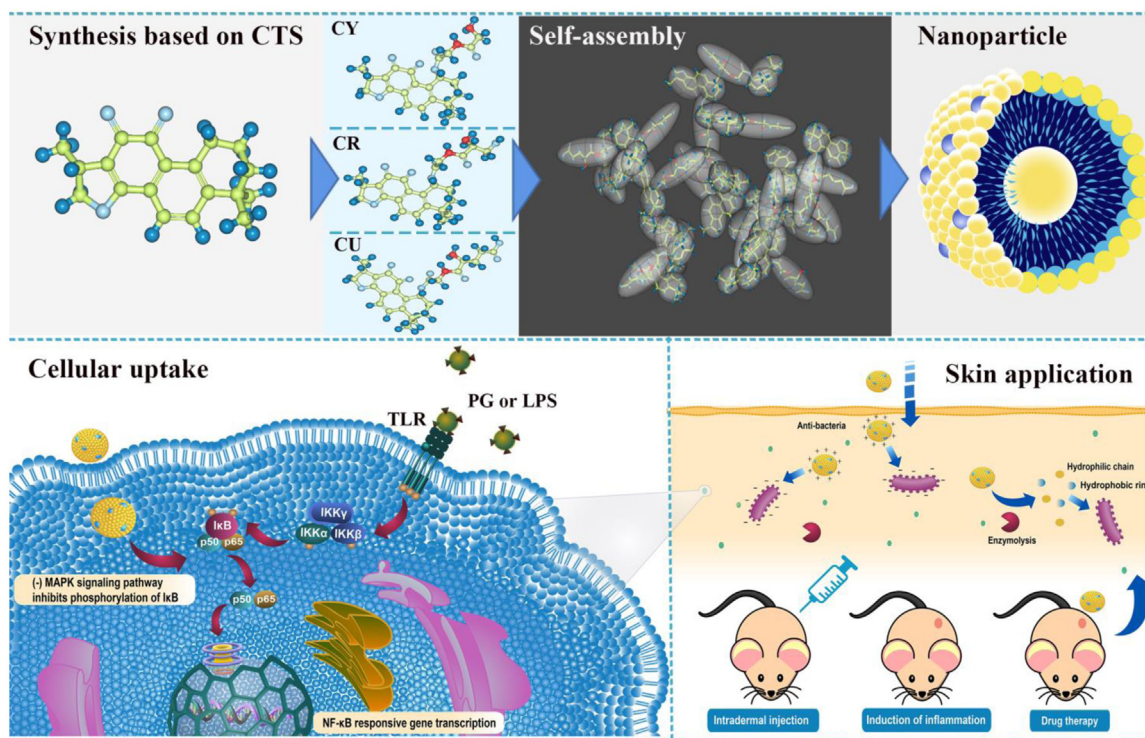
Scheme 1 – Illustration of the acne treatment using carrier-free self-assembled NPs. To begin, CTS-peptide conjugates were synthesized via chemical means, forming spherical NPs through self-assembly. Upon topical application, these self-assembled NPs swiftly penetrate the skin, effectively suppressing acne-associated bacteria like *P. acnes*. They efficiently enter HaCaT cells, where they impede the mitogen-activated protein kinase (MAPK)/nuclear factor-κB (NF-κB) signaling pathway and suppress the expression of cytokines such as TNF-α, IL-1β and IL-8. This dual-action approach combats acne by addressing both antibacterial and anti-inflammatory mechanisms. The ester bonds present within CTS-peptide conjugates facilitate their expedited degradation.

present in microbial membranes. This interaction gives rise to an electro-disruptive model referred to as the "electroporation model", leading to the disruption or disintegration of microbial cell membranes and, ultimately, the elimination of the microbes [28]. The strategic utilization of cationic short peptides as hydrophilic segment of the parent drug, not only enhances the amphiphilic attributes of the poorly soluble parent drug but also heightens its antimicrobial activity, resulting in a dual-purpose effect.

In pursuit of this objective, CTS served as the parent drug, coupled with diverse amino acid residues, resulting in three distinct CTS-peptide conjugates: CTS-G-GLY (CY), CTS-G-SER (CR), and CTS-G-GLU (CU). Their potential for developing into anti-acne Carrier-free pure drug self-assembled nanosystems was explored. The study commenced by identifying and characterizing the synthesized CTS-peptide conjugates. Subsequently, their physicochemical attributes, such as spectral data, oil-water partition coefficients, and equilibrium solubility, were investigated. Self-assembly capabilities were then assessed, encompassing parameters like assembly size, potential, polydispersity index (PDI), and microstructural morphology. Molecular dynamics (MD) simulations were employed to shed light on potential assembly mechanisms. In comparison to the dispersed form of the parent drug,

the self-assembled CY, CR, and CU nanoparticles (NPs) demonstrated noteworthy biological efficacy, showcasing improved attributes regarding skin permeability and cellular internalization efficiency. Additionally, their performance in anti-acne pharmacology was equally impressive. *In vitro* investigations unveiled elevated rates of microbial inhibition for CY, CR and CU NPs, a phenomenon likely associated with their positively charged surface structures. Moreover, these NPs significantly reduced the expression of inflammation-inducing factors like TNF-α and IL-1β in HaCaT cells, possibly achieved by modulating the Nuclear factor-κB (NF-κB) pathway. In *in vivo* study, we established a BALB/c-nu mouse acne model by intradermally injecting *P. acnes*. This approach facilitated a comprehensive assessment of various formulations, allowing us to systematically evaluate their therapeutic effects, including *in vivo* antibacterial efficacy, degree of swelling, and histological alterations. In summary, this study has successfully developed carrier-free pure drug self-assembled nanosystems utilizing CTS derivatives as the foundation. The detailed mechanism behind acne treatment is elucidated in Scheme 1. The thorough examination of diverse aspects of derivative performance provides valuable insights for the advancement of safe and effective anti-acne treatments.

2. Materials and methods

2.1. Materials

CTS (purity >95 %) was obtained from Nanjing Qiushi Biochemical Co., Ltd. BOC-glycine was purchased from Shanghai Jiuding Chemical Technology Co., Ltd. BOC-L-serine and phosphate-buffered saline (PBS, pH 5.5, 6.4 and 7.4) were obtained from Shanghai yuanye Bio-Technology Co., Ltd. BOC-D-GLU(OTBU)-OH was purchased from Beijing Wokai Biotechnology Co., Ltd. TEMPO and EDCI were purchased from Shanghai Aladdin Biochemical Technology Co., Ltd. HOBt, coumarin-6 (C6) and carbopol 940 were purchased from Shanghai Macklin Biochemical Co., Ltd. High-glucose Dulbecco's modified Eagle medium (DMEM-high), trypsin (0.25 %) and penicillin were obtained from Gibco BRL Co., Ltd., USA. Polyethylene glycogen I (PEG 400), cell counting kit-8 (CCK-8) and lipopolysaccharide (LPS) were from Beijing Solarbio science Technology Co., Ltd. TNF-α enzyme-linked immunosorbent assay (ELISA) kit, IL-1β ELISA kit, and IL-8 ELISA kit were obtained from CUSABIO (Wuhan). BAY11-7085 was from TargetMol Co., Ltd., USA. Paraformaldehyde solution (4 %) was purchased from Beijing Leagene Biotechnology Co., Ltd. Mouse anti-NF-κB (p65) antibody and MAPK antibody were obtained from Cell Signaling Technology (USA).

2.2. Physicochemical properties of the CTS-peptide conjugates

2.2.1. UV–Vis absorption and fluorescence spectrum
The drugs were dissolved directly in anhydrous ethanol and diluted to sample solution with a concentration of 0.5 mg/ml. The samples were scanned at wavelengths of 250–800 nm using a UV–vis spectrophotometer (UV–Vis; Shimadzu, 2600, Hong Kong). Test conditions: quartz cuvette 1 cm×1 cm in size, 25 °C test temperature, and 3 ml test liquid. A fluorescence spectrophotometer (Waters, Prep 150, USA) was used to test the emission spectra of each drug at the excitation wavelength of 456 nm and the excitation spectrum at the emission wavelength of 561 nm. Test conditions: quartz cuvette size of 1 cm×1 cm, test temperature of 25 °C, and volume of test liquid of 3 ml.

2.2.2. Equilibrium solubility
Excess amounts of CTS, CY, CR and CU were taken and placed in a glass vial with 10 ml solution medium. The solution media included distilled water, saline, saline/PEG 400 (4:1, v/v), and PBS (pH 4.0, 5.5, 6.4 and 7.4). Each glass vial was placed in a constant temperature shaker at 25 °C for 24 h. After dissolution equilibrium, the sample was taken, passed through a 0.22 µm nylon filter membrane and then diluted with methanol to determine the content by high-performance liquid chromatography (HPLC, in Supplementary materials).

2.2.3. Oil-water distribution coefficient
Excess amounts of CTS, CY, CR and CU were dissolved in pre-saturated n-octanol and centrifuged at 3,000 rpm for 10 min after standing, 0.5 ml supernatant was drawn into a centrifuge tube, 9 ml water saturated with n-octanol was added, and

equilibrated in a constant temperature water bath at 25 °C for 24 h. The lower aqueous phase was centrifuged at 3,000 rpm for 10 min after standing, and the concentration of each drug was determined by HPLC. In addition, a saturated solution (0.5 ml) of each drug was initially dissolved in octanol-saturated water and diluted 1,000 times with methanol. The initial solubility of each drug was determined according to HPLC. The oil-water partition coefficients (Papp and logP) of each drug were calculated according to Eq. 1.

$$Papp = \frac{\rho_0 V_0 - \rho_w V_w}{\rho_w V_w} \tag{1}$$

Where, ρ_0 represents the initial concentration of drug in water-saturated n-octanol, V_0 represents the volume of water-saturated n-octanol, ρ_w represents the concentration measured in the lower aqueous phase at drug partition equilibrium, and V_w represents the volume of water-saturated n-octanol.

2.3. Preparation and characterization of self-assembled NPs

2.3.1. Preparation of self-assembled NPs
CY, CR and CU were weighed 10 mg each, individually added to 10 ml distilled water, sonicated for 10 min, and then centrifuged at 8,000 rpm for 10 min. The supernatant obtained was the self-assembled NPs of each sample. In addition, mixed NPs (CY-C6, CR-C6 and CU-C6) containing C6 were prepared by the same method for experiments examining the NPs distribution, and the ratio of C6 to each conjugate was 1:5.

2.3.2. Particle size, PDI and zeta potential and morphology
The different self-assembled NPs were diluted 5 times with distilled water, and their particle size and PDI were determined by dynamic light scattering (DLS; Worcestershire,). Zeta potential measurements were performed directly on the undiluted NPs samples using Zetasizer Nano-ZS90 (Malvern, UK). The prepared self-assembled NPs were taken 10 µl drops onto a carbon film copper mesh, dried under an infrared lamp, and observed and photographed by transmission electron microscopy (TEM; HITACHI, H-7650, Japan).

2.4. Molecular dynamics simulation

MD simulations of self-assembled NPs were performed using Materials Studio 2019 software [29]. The spatial structures of CY, CR and CU were optimized by density functional theory (DFT). 20 DFT-optimized CY, CR and CU were dispersed in 1,000 H_2O molecules, respectively, to construct the box of each drug with water. The force field was chosen as COMPASS force field, and the initial energy was minimized by the steepest descent method. The system was first annealed at NVE synthesis (298 K-500 K) for 20 ps, and then MD simulations were performed at NVT synthesis (298 K) for 1,000 ps, and the particle grid Ewald method was used to calculate the electrostatic interactions. Meanwhile, the cut-off distance for truncated non-bonded interactions was 12.5 Å.

2.5. In vitro permeation of self-assembled NPs

2.5.1. Quantitation of the drug penetration

Six-week-old male BALB/c-nu nude mice were dislocated and executed, and the dorsal skin was carefully peeled and subcutaneous tissue was removed. The isolated skin was rinsed with saline, blotted dry with filter paper, and used immediately for *in vitro* permeation experiments. All animal experiments were conducted following the guidelines set forth by the Chinese Ministry of Science and Technology and received approval from the Ethics Committee of Southern Medical University.

The permeability assessments of the various formulations were conducted using a Franz diffusion cell system. The receptor chamber had a volume of 15 ml, and the diffusion area was 1.54 cm^2, ensuring the maintenance of a sink condition. Fresh mouse skin was positioned between the donor cell and receptor cell, with the stratum corneum facing upward. The receiver solution, composed of saline and PEG 400 (4:1, v/v), was pre-warmed to 37 °C and maintained at 350 rpm in the Franz diffusion cell. Subsequently, 0.5 ml CTS solution, CY NPs, CR NPs or CU NPs was applied on the skin. 1 ml the receiver solution was taken from the receptor chamber at regular intervals (0.5, 1, 2, 4, 6, 8, 10, 12, 24, 48 h) for HPLC analysis, and supplemented with the same volume of medium. After 48 h, the skin was taken out, washed with PBS, and then segmented into pieces. These skin segments were subjected to methanol extraction, followed by filtration through a 0.22 µm membrane. Subsequently, the extracted samples were analyzed by HPLC to determine the quantity of drug retained within the skin.

2.5.2. Visualization of the penetration

In this section, C6 was used to prepare C6-loaded NPs (CY-C6, CR-C6, CU-C6) with CY, CR or CU because of the weak fluorescence of CTS and CTS-peptide conjugates in Confocal laser microscope (CLSM) analysis. Skin samples were processed similarly to quantitative skin penetration studies. After 6 h, skin samples were carefully extracted, rinsed with PBS, and subsequently fixed in 4 % paraformaldehyde. Following fixation, the skin samples were sliced into sections with a thickness of 6 µm using a Cryostat slicer (Thermo Cryotome E, America). The penetration of C6 into the skin was then observed using a CLSM (ZEISS, CLSM 880, Germany) with an emission wavelength of 475 nm. Furthermore, to better assess the penetration ability of each formula through the skin, the average fluorescence intensity of the skin in each group was calculated using ImageJ software.

2.6. Esterase-sensitive degradation

CY, CR and CU NPs were individually dissolved in pH 6.4 PBS and configured to 200 µg/ml. In addition, pseudomelanoside lipase was dissolved in pH 6.4 PBS and diluted to 40 units/ml. The configured self-assembled NPs solution was mixed with the lipase solution (1:1, v/v) and incubated in a water bath at 37 °C [4]. Samples were taken at 0.5, 1, 2, 4, 8, 12 and 24 h, diluted with methanol, and the drug concentration was determined by HPLC after passing through a 0.22 µm microporous membrane.

To investigate the effect of enzyme concentration on the degradation of self-assembled NPs, 200 µg/ml of CY, CR and CU NPs solutions were mixed with 20, 40 and 80 units/ml of enzyme solution (1:1, v/v), respectively, and incubated in a water bath at 37 °C. After 24 h, the incubation solution was diluted with methanol, passed through a 0.22 µm microporous filter membrane, and the drug concentrations in each sample were determined by HPLC.

2.7. Cellular experiments

2.7.1. Cell culture

HaCaT cells (provided by the School of Traditional Chinese Medicine, Southern Medical University, China) were cultured in 75 cm^2 flask under standard conditions (37 °C, 5 % CO$_2$, 100 % humidity) in DMEM medium supplemented with 10 % (v/v) FBS and 1 % (v/v) penicillin.

2.7.2. Cytotoxicity test

To evaluate the cytotoxicity of each formulation, HaCaT cells were seeded in 96-well plates at a density of 5×10^3 cells per well. After 24 h of incubation, the cells were treated with CTS, CY, CR or CU for 24 h at concentrations ranging from 400 µmol/l to 12.5 µmol/l, and the untreated cells were set up as a negative control. After continuing incubation for 24 h, each well was replaced with new medium and incubated with 10 % CCK-8 solution for 2 h. Finally, the absorbance OD at 450 nm was measured using a microplate reader (Thermo Fisher Scientific, Fl-01620 Vantaa, Finland) to calculate the cell survival rate.

2.7.3. Anti-inflammatory activity

HaCaT cells were seeded in a 6-well plate at a density of 2×10^5 cells/well and precultured until cell growth covered 80 % of the wells and then given different treatments depending on the group. Control group cells were cultured with medium for 36 h. LPS group (Model) cells were first cultured with medium for 12 h and then cultured to 1 µg/ml LPS solution for 24 h. For the treatment group, cells were cultured with CTS, CY, CR, CU or BAY11–7085 (5 µmol/l) for 12 h, followed by 1 µg/ml of LPS solution for 24 h. Finally, the cell culture supernatants were collected and the expression of TNF-α, IL-1β and IL-8 in the supernatants was measured by ELISA kits.

Meanwhile, to investigate the mRNA expression of relevant inflammatory factors in HaCaT cells, cellular total mRNA was extracted with 1 ml Triol lysate for reverse transcription polymerase chain reaction (RT-PCR). The concentration of mRNA in the final extraction solution was determined using a Spectrophotometer (Thermo Scientific, NanoDrop 2000, America). The RNA was transcribed into cDNA by PrimeScript RT Master Mix (Takara, RR036A, Japan), followed by DNA amplification by TB Green Premix Ex Taq (Takara, RR420A, Japan). PCR was performed using the Real-Time PCR detection system (BIOER, FQD-96A, China). The primers (Sangon Biotech, China) used for PCR are listed in Table S2.

2.7.4. Cellular uptake

For flow cytometry analysis, HaCaT cells were seeded in 6-well plates at a density of 1×10^5 cells/well and allowed to grow overnight. Subsequently, the cells were incubated with CY-C6, CR-C6, CU-C6, or C6 solution (2.5 µg/ml for C6) for 2 h. Following this incubation, the cells were trypsinized, resuspended in 1 ml of PBS, and subjected to flow cytometry analysis (BD, LSRFortessa X-20, USA).

Meanwhile, in order to quantitatively determine the uptake of each formula by HaCaT, the cells were seeded in 6-well plates at a density of 1×10^5 cells/well and allowed to grow overnight. Subsequently, the cells were incubated with CY, CR, CU NPs or CTS solution (20 µmol/l for each drug) for 2 h. Following this incubation, the cells were thoroughly washed 3 times with PBS. Then, the cells were lysed with 1 ml Triton X-100, and ultrasound was performed while keeping the samples on ice. The lysed cell fluid was subsequently centrifuged at 67,000 g for 5 min, and the supernatant (20 µl) was subjected to HPLC analysis.

2.7.5. Intracellular distribution

HaCaT cells were cultured in well of confocal dishes (10 mm diameter) at a density of 1×10^4/well for 24 h. The cells were then treated with CY-C6, CR-C6, CU-C6 or C6 solution (2.5 µg/ml for C6) for 4 h, respectively. After washed with PBS, the cells were fixed with paraformaldehyde solution (4 %, w/v) for 15 min followed by rinsing with PBS. Finally, cells were stained with 1 µg/ml of DAPI for 15 min to locate the nucleus, after which they were visualized with CLSM (ZEISS, CLSM 880, Germany).

2.8. In vitro anti-bactericidal effect

2.8.1. Acne-associated bacteria culture

P. acnes (GDMCC 1.243) was cultured on Reinforced Clostridial Agar/Broth Medium (RCM) at 37 °C in an anaerobic environment. Sau. (GDMCC 1.1220) and Sep. (GDMCC 1.143) were cultured on NA medium at 37°C. All microorganisms used in this study are purchased from the Guangdong Microbial Strain Conservation Centre (GDMCC) (Guangzhou, China).

2.8.2. Minimum inhibition concentration (MIC)

CTS was dissolved in DMSO/saline (1:9, v/v), while CY, CR and CU NPs were diluted directly with pure water, and all formulations were configured into 1 µmol/ml sample solutions. Next, sample solutions were diluted with LB or RCM broth gradients to different multiples of dilutions (1:1 to 1:256, v/v) and incubated with P. acnes, Sau. or Sep. (1.5×10^6 CFU/ml) for 48 h. Microbial growth was finally observed.

2.8.3. Inhibition zone

CTS, CY, CR and CU were prepared as 10 µmol/ml sample solutions according to the same method as MIC and set aside. P. acnes, Sau. and Sep. were diluted to 1.5×10^8 CFU/ml in saline after 3 generations of culture and spread evenly on the RCM or NA solid medium. 6 mm round paper plates were placed on the surface of the solid medium using forceps. Afterward, 10 µl the above-configured sample solution was added dropwise to the paper plates, where

the control was added with DMSO/saline (1:9, v/v). All solid mediums were incubated at a constant temperature of 37 °C for 48 h (P. acnes was incubated in an anaerobic environment) before measuring the diameter of the inhibition zone.

2.9. In vivo study

2.9.1. Establishment and treatment of P. acnes infection model

In vivo experiments were conducted using healthy six-week-old male BALB/c-nu mice. Mice were acclimatized and fed in a suitable environment for 3 d before the experiments. Except for the blank group, 1.5×10^8 CFU/ml P. acnes solution was injected intradermally into the dorsal skin of nude mice daily at a dose of 0.05 ml/10 g (mice's body weight). After 7 d, mice that had successfully induced inflammation in dorsol skin were randomly divided into 3 groups ($n = 6$): (1) Control group (no treatment), (2) CTS treatment group, and (3) CU treatment group. In addition, male mice of the same age without inflammation induction were used as a blank group. In this study, CU was selected as a representative self-assembled NPs for in vivo anti-acne studies in view of its better in vitro evaluation results, such as antibacterial activity, self-assembly properties, etc. Moreover, both CTS and CU were configured as a 1 mg/ml hydrogel (Carbopol 940) when administered to animals.

The hydrogels were applied at a dose of 0.05 g/10 g (mice's body weight) to the inflamed area in the CTS or CU group, respectively, while the blank and control groups were left untreated.

The swelling of the inflamed area was then observed daily and the dorsal skin of the nude mice was photographed on Days 1, 3, 5 and 7 of treatment. The length and width of the swollen area were also measured with vernier calipers, and the skin volume was calculated according to Eq. 2 [30], in which a and b represent the length and width, respectively.

$$V = \frac{a \times b^2}{2} \tag{2}$$

2.9.2. In vivo antibacterial efficiency

At the end of treatment, skin samples were obtained from each group of mice using a sterile skin biopsy punch (8 mm). The skin samples were homogenized in 2 ml of PBS. The slurries were diluted 10 times and 0.1 ml them were applied to RCM solid mediums, followed by incubation at 37 °C for 48 h (anaerobic environment). The number of colonies formed in each medium was recorded and the in vivo bacterial inhibition efficiency of each hydrogel (treatment vs control group, %) was calculated.

2.9.3. Histomorphological observation

The harvested dorsal skin specimens were fixed in 4 % (w/v) paraformaldehyde solution for 24 h, followed by sectioning into 4 µm thick paraffin sections. These sections were subsequently stained with hematoxylin and eosin and then captured using a digital section scanner (KFBIO, Kf-pro-020, China).

2.9.4. Immunohistochemical observation

To investigate the anti-inflammatory effects of each formulation *in vivo*, paraffin sections were incubated with mouse anti-NF-κB p65 antibody (1:400, CST, USA) and MAPK antibody (1:400, CST, USA) to evaluate the expression of both proteins in the skin. Additionally, in order to better comprehend the differences in the expression of inflammation-related proteins among the groups, the Average Density (AOD) of the skin in each group was calculated using ImageJ software.

2.10. Data analysis

Results were presented as mean $\pm$ SD. SPSS 21.0 software (SPSS, Chicago, USA) was employed. All statistics were analyzed using one-way ANOVA with $P < 0.05$ as the criterion of significance.

3. Results and discussion

3.1. Synthesis and characterization of CTS-peptide conjugates

The design of carrier-free pure drug self-assembled nanosystems necessitates careful consideration of several critical factors [31]: (1) the feasibility of modifying the parent drug; (2) the potential for self-assembly of the conjugate; and (3) the conjugate's capability to undergo metabolism and elimination within an endogenous environment.

To begin with, the chemical modification of the parent drug typically hinges on the presence of suitable functional groups. However, CTS presents a challenge due to its limited sites available for modification, and its active sites responsible for anti-inflammatory, antioxidant, and antimicrobial effects, notably the adjacent quinone and dihydrofuran ring structures on the hexacyclic ring [32], are generally conserved. Consequently, we opted to target the C-1 position on the parent ring for nucleophilic substitution reactions, yielding the intermediate compound CTS-G. Subsequently, we conducted amide condensation to elongate the hydrophilic chain, resulting in the amphiphilic derivatives CY, CR and CU. A comprehensive outline of the synthesis procedure can be found in Method S1, and visual representations are provided in Fig. S1-S4 (All in Supplementary materials).

The nucleophilic substitution at the C-1 position represents a pivotal step, leading to a reduction in the count of C1-H from 2 to 1 and inducing alterations in the chemical milieu, discernible via proton nuclear magnetic resonance (^{1}H NMR) spectroscopy. As depicted in Fig. 1A, the chemical shift (δ) of C1-H in CTS registers at 3.20, manifesting as a triplet due to its interaction with C2-H. In the case of the derivative CU, the C1-H chemical shift experiences upfield shifting, with δ escalating to 6.37, attributable to the deshielding effect induced by the substituent. Notably, since both C1-H positions in CTS possess an equal likelihood of substitution, CU manifests both R and S configurations, resulting in the appearance of two closely situated triplets in the ^{1}H NMR spectrum. Additionally, CY and CR exhibit a

similar pattern, with their C1-H signals peaking around 6.50. The ^{1}H NMR spectra for CTS and CTS-peptide conjugates are provided in Fig. S5-S8.

The ^{1}H NMR outcomes definitively validate the successful attachment of amino acid residues at the C-1 position of cryptotanshinone. To further ascertain the structural composition of the products, high-resolution mass spectrometry (HRMS) analyses were conducted. As delineated in Figs. 1B and S9, CTS ionized to [M+Na]+, displaying a molecular formula of $C_{19}H_{20}O_3Na$, while CY, CR and CU ionized to [M+H]+, denoting respective molecular formulas of $C_{23}H_{27}N_2O_6$, $C_{24}H_{29}N_2O_7$, and $C_{26}H_{31}N_2O_8$. HRMS results affirm the alignment of the molecular formulas of the products with initial expectations.

Alterations in the characteristic peaks of functional groups within the CTS-peptide conjugates subsequent to derivatization were meticulously examined via fourier-transform infrared spectroscopy (FTIR). In comparison to CTS, the CTS-peptide conjugates exhibit more pronounced signal peaks in the spectral range spanning from 3250 cm^{-1} to 3600 cm^{-1}. This heightened intensity arises from the stretching vibrations of N–H groups in the derivative side chains and intermolecular hydrogen bonding. Furthermore, more prominent stretching vibrations of C–N around 1200 cm^{-1} and C=O within the vicinity of 1650 cm^{-1} to 1680 cm^{-1} substantiate the formation of amide bonds, corroborating our initial expectations (Fig. 1C). Moreover, CU exhibits a more robust characteristic peak signal within the spectral region of 3250 cm^{-1} to 3600 cm^{-1} in comparison to the other two derivatives, potentially attributed to the presence of additional carboxyl groups.

In summary, the structures of the synthesized CTS-peptide conjugates were successfully identified through a combination of ^{1}H NMR, HRMS, and FTIR analyses.

3.2. Preparation and characterization of self-assembled NPs

Preliminary experiments have unequivocally verified the spontaneous self-assembly of the three CTS derivatives in an aqueous medium (Fig. S10). To elucidate the microstructural morphology of the fabricated Carrier-free pure drug self-assembled nanosystems, we conducted TEM examinations. The findings unequivocally demonstrate that they self-organize into spherical nanoparticles of varying dimensions (Fig. 1D).

Subsequently, DLS measurements were employed to quantify these nanoparticle sizes and PDI (Table S3). CY NPs exhibited a mean diameter of 494.4 $\pm$ 17.4 nm, accompanied by a PDI of 0.45 $\pm$ 0.02 (Fig. 1E and 1F). CR NPs displayed a diameter of 367.1 $\pm$ 15.6 nm, coupled with a PDI of 0.46 $\pm$ 0.03. Remarkably, CU NPs exhibited a smaller and more uniform particle size, measuring 155.4 $\pm$ 5.9 nm with a PDI of 0.33 $\pm$ 0.02. It is noteworthy that CU NPs carried a stronger surface charge, with an electric potential measuring as high as 33.27 $\pm$ 1.72 mV (Fig. 1E). This heightened charge may be attributed to the amphoteric ionization properties of CU, while CY and CR NPs displayed relatively weak positive surface charges, likely due to the presence of free amino groups.
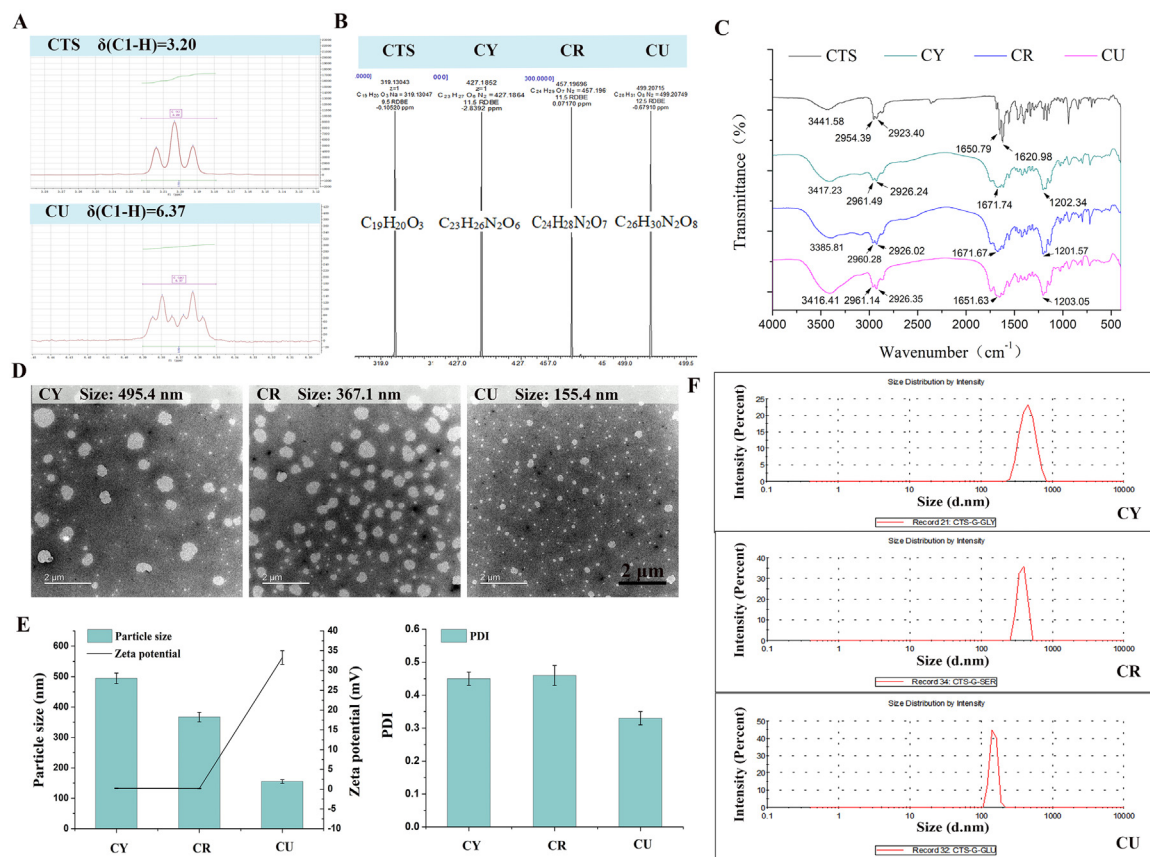
Fig. 1 – (A) Characteristic ^{1}H NMR signal peaks, **(B)** HRMS fitted -molecular formulas, and **(C)** FTIR spectra of CTS and its derivatives. **(D)** TEM images of CY, CR and CU NPs. **(E and F)** Particle size, zeta potential, and PDI values of the NPs, (n = 3).

Furthermore, the C6-loaded NPs and non-loaded NPs exhibit similarity in terms of particle size, PDI, and zeta potential.

To obtain a more comprehensive understanding of the assembly mechanism of self-assembled NPs, we employed MD simulations to investigate the intermolecular interactions occurring during the assembly process. As illustrated in Fig. 2A, the majority of CY molecules aggregated in water, forming spherical supramolecular assemblies, while others remained dispersed either individually or in smaller clusters. Within the CY assembly system, a total of 6 pairs of intermolecular hydrogen bonds were identified, with lengths ranging from 1.964 to 2.380 Å and angles from 131.99° to 164.30°, along with 3 pairs of water-bridged hydrogen bonds (Fig. 2B). Furthermore, the system displayed instances where two or more CY molecules aligned vertically or coplanarly (Fig. 2C), suggesting that these regular three-dimensional arrangements were likely induced by the π-π stacking interactions occurring within the aromatic rings of CY molecules.

In contrast to CY, CR exhibited more prominent aggregation in water, leading to the formation of uniformly spherical supramolecular assemblies (Fig. 2D). The CR assembly system comprised a total of 20 pairs of intermolecular hydrogen bonds, with lengths ranging from 1.576 to 2.506 Å and angles from 129.30° to 176.91°, 1 pair of intramolecular hydrogen

bonds (with a length of 2.346 Å and an angle of 129.30°), and 4 pairs of water-bridged hydrogen bonds (Fig. 2E). Similar to CY, CR molecules arranged themselves in a three-dimensional configuration influenced by π-π stacking (Fig. 2F). Taking the particle size and PDI results into consideration (Fig. 1E), it is postulated that the smaller sizes and lower PDI of CR NPs compared to CY NPs may be attributed to the formation of a greater number of intermolecular hydrogen bonds and water-bridged hydrogen bonds during the aggregation of CR molecules.

As for CU, its supramolecular assemblies exhibit a ribbon-like morphology, suggesting their potential for fiber formation (Fig. 2G). Nevertheless, it's important to note that in this study, we did not conduct an in-depth investigation into this aspect. Within the CU system, a total of 8 pairs of intermolecular hydrogen bonds were identified, with lengths ranging from 1.992 to 2.372 Å and angles from 123.53° to 161.82°. Additionally, 4 pairs of intramolecular hydrogen bonds were observed, with lengths ranging from 1.741 to 2.498 Å and angles from 121.34° to 149.86°. Furthermore, 4 pairs of water-bridged hydrogen bonds were also identified (Fig. 2H). When we consider the analysis of particle size and PDI results (Fig. 1E), it becomes evident that CU NPs have significantly smaller particle sizes and lower PDI compared to CY and CR NPs. This phenomenon is likely attributed to
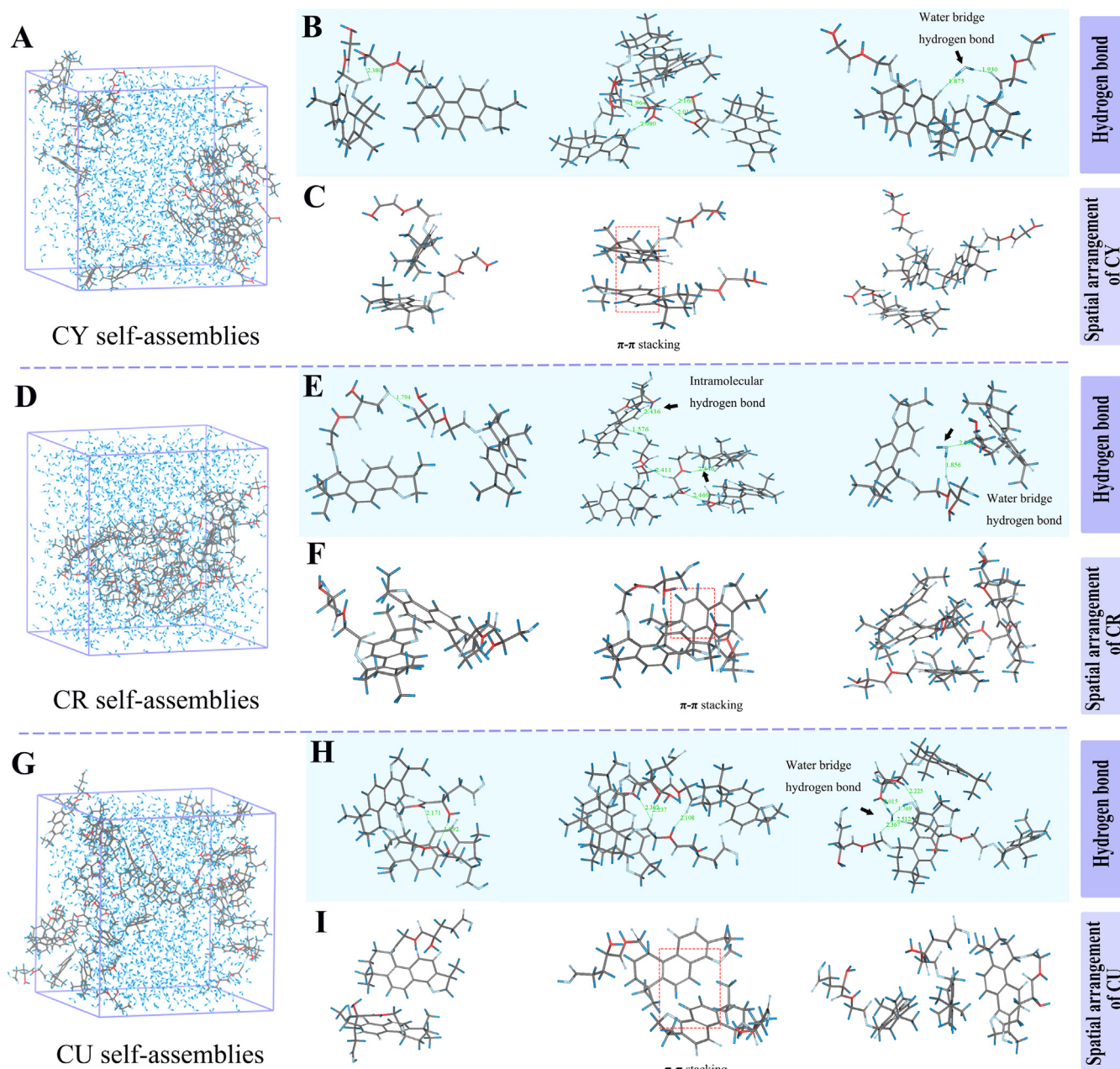
Fig. 2 – (A) MD simulation images of self-assembled NPs for each CTS derivative. Self-assembly morphology, (B) hydrogen bonding interactions, and (C) spatial arrangements of GY. (D) Self-assembly morphology, (E) hydrogen bonding interactions, and (F) spatial arrangements of CR. (G) Self-assembly morphology, (H) hydrogen bonding interactions, and (I) spatial arrangements of CU.

the presence of a greater number of intramolecular hydrogen bonds within the system, allowing for the self-assembly of fewer CU molecules. Similar to CY and CR, the arrangement of CU molecules is also influenced by π-π stacking interactions (Fig. 2I).

In addition to the hydrogen bonds and π-π stacking, a significant number of hydrophilic interactions between CY, CR or CU molecules and water have been observed (Fig. S11). This implies that hydrophobic interactions play a substantial role in enhancing the stability of self-assembly in these compounds. The findings suggest that CY, CR and

CU likely promote molecular aggregation and assembly through hydrogen bonds and water-bridged hydrogen bonds, while also reinforcing their interior via π-π stacking and hydrophobic interactions. Ultimately, these interactions contribute to the formation of specific three-dimensional structures.

3.3. Quantitative analysis of CTS-peptide conjugates

To facilitate the quantitative analysis of CTS-peptide conjugates, we performed UV spectroscopy on both CTS
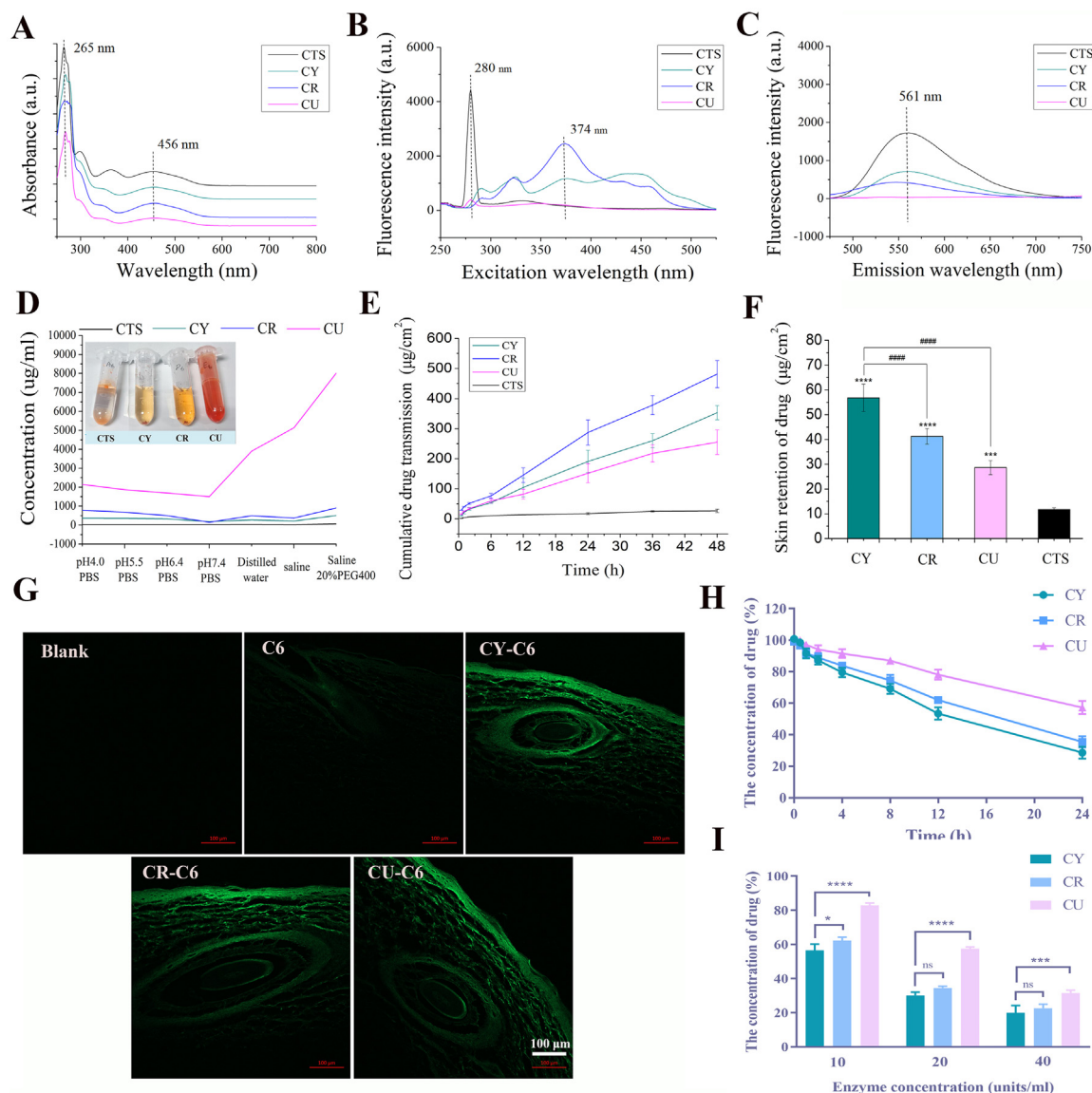
Fig. 3 – (A) UV absorption spectra, **(B)** fluorescence excitation spectra, **(C)** fluorescence emission spectra, and **(D)** solubility of CTS and its derivatives. **(E)** Cumulative drug transmission and **(F)** skin retention of CTS and self-assembled NPs (***$P < 0.001$, **** $P < 0.0001$ vs CTS, ####$P < 0.0001$ vs CY, $n = 3$). **(G)** The delivery pathway of loaded C6 NPs through mouse skin; scale bar is 100 μm. **(H)** Degradation curves of self-assembled NPs within 24 h and **(I)** degradation under different enzyme concentrations (*$P < 0.05$, ***$P < 0.001$, ****$P < 0.0001$, $n = 3$).

and its derivatives. As illustrated in Fig. 3A, the characteristic absorption wavelengths of CTS lie at 265 nm and 456 nm within the 250–800 nm range. Remarkably, CY, CR and CU displayed absorption bands at positions and with shapes closely resembling those of CTS at 265 nm and 456 nm. This observation suggests that the C-1 modification of CTS does not exert a substantial influence on the conjugated structures within the core molecule, which are responsible for its pharmacological activity.

Following this, all samples underwent excitation light scanning at 265 nm and 456 nm, yielding excitation spectra (Em = 561 nm, Fig. 3B) and emission spectra (Ex = 456 nm, Fig. 3C). In Fig. 3C, the fluorescence peak of CTS is evident at 561 nm. However, upon derivatization, there was a notable

decrease in the intensity of spectral peaks for CY, CR and CU, with CU exhibiting a particularly minimal fluorescence peak. Fig. 3B reveals that CTS exclusively emits fluorescence when excited at Ex=280 nm, whereas CY and CR display multiple excitation signal peaks. Importantly, the excitation signal peak of CU is exceedingly weak. From the fluorescence spectra, it becomes apparent that the C-1 substitution of CTS significantly affects its fluorescence properties. As a result, fluorescence analysis is not suitable for the quantitative determination of CTS-peptide conjugates. Ultimately, we conducted content determination analysis using an HPLC, relying on the characteristic UV absorption of CTS and its conjugates at 265 nm. Comprehensive HPLC chromatograms for each drug are available in Fig. S12.

3.4. Skin penetration of self-assembled NPs

In the context of *in vitro* permeation experiments, it is imperative that the drugs demonstrate a certain level of solubility within the receiving solution of the Franz diffusion cell to establish sink conditions. This ensures the smooth progression of the experiments. Consequently, in this study, we conducted an investigation into the equilibrium solubility of CTS and its derivatives in various solvents (Table S4).

As depicted in Fig. 3D, when distilled water served as the solvent, the solubility of the drugs followed a descending order of CU > CR > CY > CTS. This trend suggests that as the proportion of hydrophilic components in the chemical structure increases, the solubility of the drugs also proportionally rises. Noteworthy is the substantial increase in solubility observed for CY and CR, which reached levels 10 times and 18 times that of CTS, respectively. Moreover, the solubility of CU in water showed a significant spike, reaching 149 times that of CTS, with a final value of 3.90 mg/ml. This result could potentially be attributed to the amphoteric nature of CU, rendering it more susceptible to ionization in aqueous environments.

With the sole exception of a physiological saline solution (containing 20 % PEG400), CTS exhibited markedly low solubility in all other tested solutions. Consequently, the selection of a receiving solution containing 20 % PEG 400 in the Franz diffusion cell was driven by this observed solubility profile for *in vitro* permeation experiments.

Beyond solubility, the oil-water partition coefficient of a drug also exerts a direct influence on its skin permeation [33-35]. The skin, being the body's largest organ, encompasses the stratum corneum, epidermis, dermis, and subcutaneous tissue in an outer-to-inner arrangement. The lipid-rich stratum corneum facilitates the passage of highly lipophilic drugs, whereas the epidermis and dermis predominantly consist of hydrophilic tissues, rendering the penetration of highly lipophilic drugs challenging. Consequently, for a topical dermatological drug, it must possess an appropriate oil-water partition coefficient, typically falling within a logP range of 1 to 3, to enable smooth ingress into the skin, as dictated by the skin's inherent structural characteristics [36,37]. As delineated in Table S5, CTS exhibits a logP value of 4.49 in octanol/water system. In contrast, CY, CR and CU demonstrate logP values of 1.27, 1.14 and 2.88, respectively. A noteworthy reduction in the *logP* values of all CTS-peptide conjugates, in comparison to CTS, is evident. Moreover, with the increasing proportion of hydrophilic components in the derivative structures, the logP values consistently decrease, except for CU. Despite the additional carboxylic acid groups and substantially heightened solubility (Fig. 3D) relative to other derivatives, the logP of CU value does not reach the lowest level. In contrast to other derivatives, CU exhibits properties more akin to amphiphilic compounds. Cumulatively, these findings suggest that CY, CR and CU theoretically possess a greater proclivity for skin penetration.

Following this, we conducted *in vitro* penetration experiments to substantiate this claim. As illustrated in Fig. 3E, the findings demonstrate a substantial escalation in the unit cumulative transmission quantities of CY, CR and CU at 48 h ($P < 0.0001$ vs CTS), reaching 13.4-fold, 18.2-fold, and 9.7-fold that of CTS, respectively. Moreover, a correlation in unit cumulative permeation amounts was observed, with CR>CY>CU, aligning with the logP outcomes. Regarding skin retention (Fig. 3F), CY, CR and CU all displayed varying degrees of augmentation, reaching 4.9-fold, 3.5-fold and 2.5-fold that of CTS ($P < 0.0001$ vs CTS), respectively.

Subsequently, to visualize the process of self-assembled NPs entering the skin, we utilized CLSM for capturing skin section images. Due to the feeble fluorescence of CTS and its derivatives, C6 was employed to trace the location of the NPs as they entered the skin. The results elucidate that after 6 h treatment of formulation, C6 loaded with CY, CR or CU NPs effectively permeated beneath the epidermis, whereas dispersed C6 was solely observable in the skin's stratum corneum (Fig. 3G). This compellingly underscores the advantages of CY, CR, and CU concerning skin permeation. Furthermore, the findings imply that these CTS derivatives ingress the skin in nanoparticle form.

The CLSM quantitative results (Fig. S13) demonstrate a notable elevation in the average gray value of the skin when compared to pure C6 within each nanoparticle group, implying a substantial augmentation in the skin permeation of C6 subsequent to encapsulation by CY, CR and CU NPs. However, no significant variance was observed among the three nanoparticle groups, suggesting that the particle size exerts minimal influence on their skin penetration. This phenomenon may be attributed to the reduced number of hair follicles in nude mice, resulting in CY, CR and CU NPs predominantly traversing the skin via intracellular and intercellular pathways, with less penetration through the skin appendage pathway.

In summary, we posit CY, CR and CU demonstrate a noteworthy enhancement in local bioavailability compared to CTS when applied topically. This augmentation can likely be ascribed to their heightened solubility and more appropriate logP values. The smaller particle size also facilitates nanoparticle penetration through the follicular route, although the effect is less pronounced in nude mice. Nonetheless, it is imperative to acknowledge that despite the substantial promise exhibited by CY, CR and CU in transdermal delivery, further pharmacological investigations are imperative.

3.5. Degradation of the self-assembled NPs

Although not obligatory, the biodegradability of biomaterials or drugs retains significant importance as it relates to the metabolic load on the organism [38,39]. In this study, CTS-peptide conjugates were crafted, incorporating ester bonds, which are sensitive functional groups, into the CTS framework. Hence, the self-assembled NPs containing these ester bonds will gradually degrade under the action of lipases. Employing *in vitro* techniques to simulate an acne environment and investigate esterase sensitivity aids in comprehending the rate and ease of metabolism of various self-assembled NPs.

The investigation initially examined the degradation rate of 100 µg/ml CY, CR, and CU NPs in an aqueous solution containing 20 units/ml of pseudocholinesterase, as depicted

in Fig. 3H. Under enzymatic influence, CY displayed the swiftest degradation rate, diminishing by 71.4 % within 24 h, while CR and CU degraded by 64.6 % and 42.8 %, respectively. Experimental findings propose that a principal determinant influencing the degradation of self-assembled NPs likely resides in their steric hindrance. As the hydrophilic ends of CY, CR and CU molecules progressively elongate in molecular structure, spatial hindrance increases, rendering it more arduous for lipases to engage with the ester bonds.

Additionally, we explored the influence of enzyme concentration on these NPs degradation rates. As depicted in Fig. 3I, after a 24-h incubation with 10 units/ml of lipase, there was a noteworthy divergence in the degradation rates among these NPs. However, upon co-incubation with 40 units/ml of lipase for 24 h, all NPs experienced degradation of approximately 70 % or more. Consequently, it becomes apparent that with increasing enzyme concentration, the impact of steric hindrance on these NPs degradation rates diminishes.

It is worth noting, however, that while the aforementioned research indicates the self-assembled NPs degradation in the presence of lipases, real-world conditions feature relatively low enzyme concentrations in the skin, requiring an extended duration for degradation. This is unlikely to impede their capacity to exert their effects on bacteria or cells.

3.6.   Cell experiment

3.6.1.   Cellular uptake of the self-assembled NPs

HaCaT cells represent a primary component of the skin's stratum corneum and epidermis, and also participate in the inflammatory response phase of acne development [40]. Consequently, the efficient internalization of self-assembled NPs by HaCaT cells assumes paramount importance in facilitating their anti-inflammatory activity. The cellular uptake patterns of these NPs were evaluated using CLSM and flow cytometry, employing C6 fluorescence as a tracking marker.

As illustrated in Fig. 4A, conspicuous green fluorescence aggregates around the nuclei of HaCaT cells, signifying the effective internalization of C6. Notably, C6 encapsulated within CY, CR and CU NPs exhibited markedly higher fluorescence intensity in comparison to pure C6, underscoring the proficiency of self-assembled NPs as drug delivery systems. To complement these findings, quantitative assessments were carried out concurrently with flow cytometry analysis. As depicted in Fig. 4B, following a 2-h incubation period, free C6 exhibited negligible uptake by HaCaT cells. In contrast, CY-C6 NPs substantially bolstered C6 delivery, achieving a cellular uptake rate of 58.1 %. Furthermore, HaCaT cells exhibited cellular uptake rates of 69.1 % and 71.9 % for CR-C6 and CU-C6 NPs, respectively, surpassing the uptake rate of CY-C6. These results collectively indicate a significantly heightened rate of effective nanoparticle uptake by HaCaT cells relative to free C6.

As illustrated in Fig. S14, the HPLC results indicated a significant elevation in intracellular drug levels for CY, CR, and CU compared to the free CTS drug form ($P < 0.0001$). This improvement could be ascribed to the larger size of the

self-assembled supramolecular structures [41]. Particularly, CU demonstrated a further enhancement in cellular internalization when compared to CY and CR ($P < 0.05$ vs CY, $P < 0.001$ vs CR). We attribute this to the heightened surface charge of CU, facilitating more rapid proximity to the cell membrane and increased uptake efficiency [42]. In summary, these experiments establish that self-assembled NPs exhibit a heightened rate of cellular internalization *in vitro*, with CU NPs exhibiting superior performance.

3.6.2.   Cytotoxicity of different formulations

To evaluate the safety of self-assembled NPs, we assessed cell viability after exposure to various formulation treatments using the CCK-8 assay. As illustrated in Fig. 5A, the cytotoxicity of each nanoparticle formulation is marginally higher than that of pure CTS within the concentration range of 12.5 µmol/l to 100 µmol/l. This effect might be attributed to the alkaline amino groups present in the self-assembled NPs. Nonetheless, at concentrations below 12.5 µmol/l, all formulations demonstrated no cytotoxic effects, with cell viability exceeding 95 %, underscoring the high biocompatibility of these self-assembled NPs.

3.6.3.   Effects of different formulations on cellular inflammation

Prior investigations have already established that CTS primarily exerts its anti-inflammatory effects by modulating the MAPK/NF-κB signaling pathway, inhibiting I-κB phosphorylation, and blocking NF-κB activation [43]. The self-assembled NPs created in this study are CTS derivatives, and their anti-inflammatory efficacy necessitates further substantiation. Consequently, we conducted a cellular-level assessment to evaluate the impact of each formulation on the expression of inflammatory mediators in HaCaT cells subjected to LPS treatment. LPS was selected as the inflammatory stimulus due to its shared reliance with *P. acnes* on the Toll-like receptor 4 (TLR4) receptor located on the cell membrane for instigating inflammatory responses [44].

The experimental findings, as illustrated in Fig. 5B, demonstrate a noteworthy increase in TNF-α expression levels in HaCaT cells following LPS treatment ($P < 0.0001$ vs control), signifying the effective induction of an inflammatory response by LPS. Subsequently, cells subjected to inflammatory induction were treated with CTS, CY, CR, CU, or BAY11-7085. The results reveal varying degrees of reduction in TNF-α levels among cells treated with different formulations. Notably, BAY11-7085, an inhibitor of the NF-κB pathway, substantially suppressed TNF-α expression in the cells ($P < 0.0001$ vs LPS). Within the self-assembled NPs, CR exhibited the most potent downregulation effect against TNF-α ($P < 0.01$ vs LPS), whereas the TNF-α levels in the CTS and CU groups, although reduced, did not reach statistical significance, possibly attributed to the low expression of TNF-α in HaCaT cells.

As depicted in Fig. 5C and D, LPS similarly induced elevated expression of IL-1β and IL-8 in HaCaT cells ($P < 0.0001$, $P < 0.01$ vs control). Nevertheless, treatment with each formulation significantly attenuated the expression of IL-1β and IL-8. These collective results indicate that both CTS and self-assembled NPs possess a substantial inhibitory
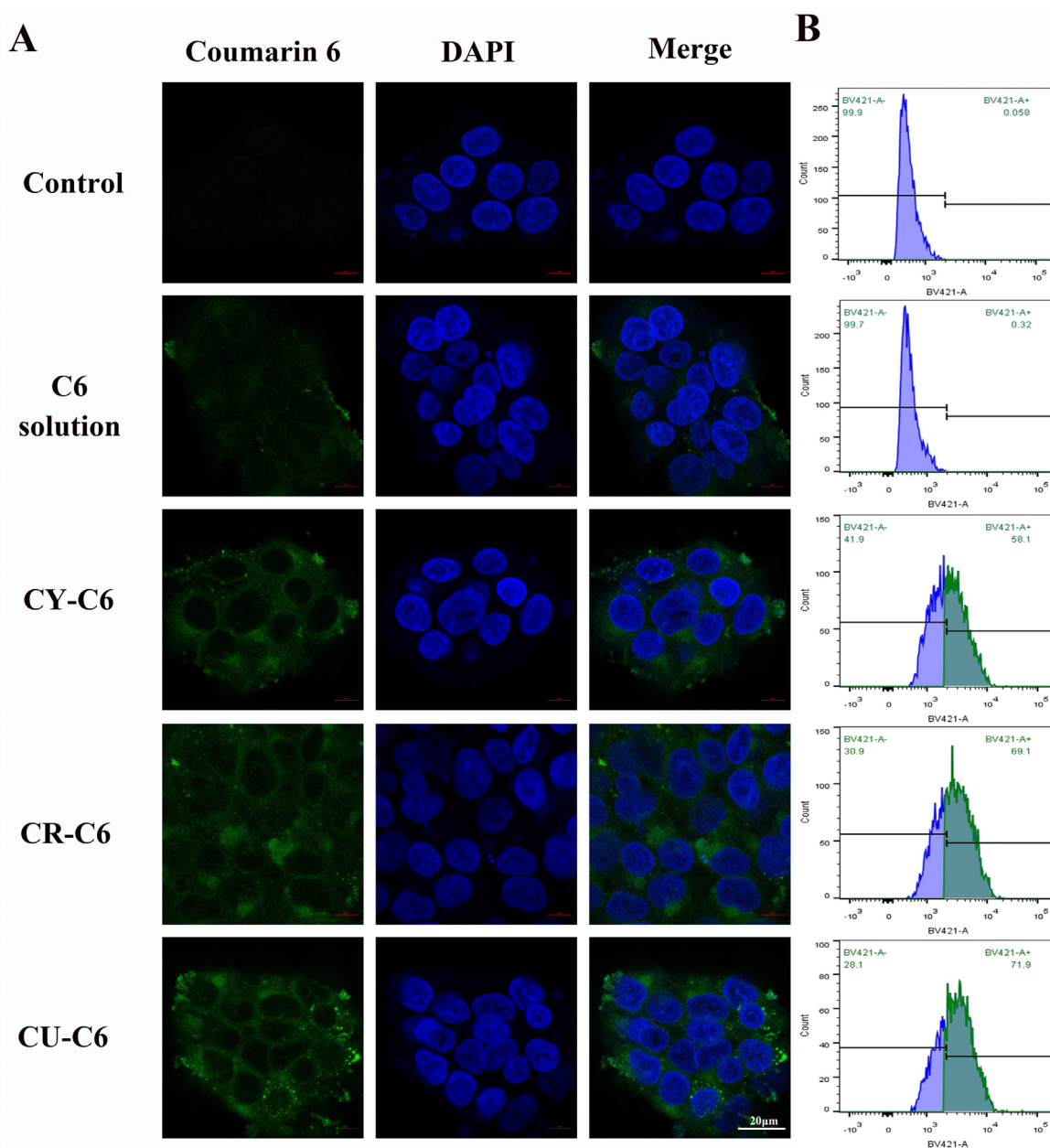
Fig. 4 – (A) Visualization of C6 uptake into HaCaT cells of C6 solution, CY-C6, CR-C6 and CU-C6 by CLSM with the scale bar at 20 μm. (B) Comparative analysis of cellular uptake of C6 from various formulations into HaCaT cells by flow cytometry.

effect on the LPS-induced inflammatory response, effectively diminishing the expression of TNF-α, IL-1β, and IL-8 in HaCaT cells, with efficacy comparable to the positive control BAY11-7085. In conjunction with the UV spectrum results (Fig. 3A), our analysis suggests that the self-assembled NPs primarily exploit the anti-inflammatory activity of the CTS core and, akin to CTS, downregulate the expression of inflammatory factors by inhibiting the NF-κB signaling pathway.

To further corroborate the anti-inflammatory effects of various formulations, we conducted an assessment of the mRNA expression of inflammatory factors using RT-PCR. The experimental findings, depicted in Fig. 5E, reveal that subsequent to LPS induction, there was a marked elevation in the mRNA expression levels of TNF-α, IL-

1β, and IL-8 within the cells when compared to baseline levels. Nevertheless, following treatment with different formulations, the expression of these inflammatory factors' mRNA exhibited varying degrees of reduction. In particular, TNF-α mRNA displayed a significant upregulation in the LPS group ($P < 0.0001$ vs control). However, in the CY group, it decreased to levels akin to the positive control BAY11–7085, effectively normalizing its expression. The remaining formulations also significantly downregulated TNF-α mRNA expression, with no statistically significant differences discerned among them (Fig. 5F). As illustrated in Fig. 5G, IL-1β mRNA exhibited a similar significant upregulation following LPS induction ($P < 0.0001$ vs control). Subsequently, after treatment with different formulations
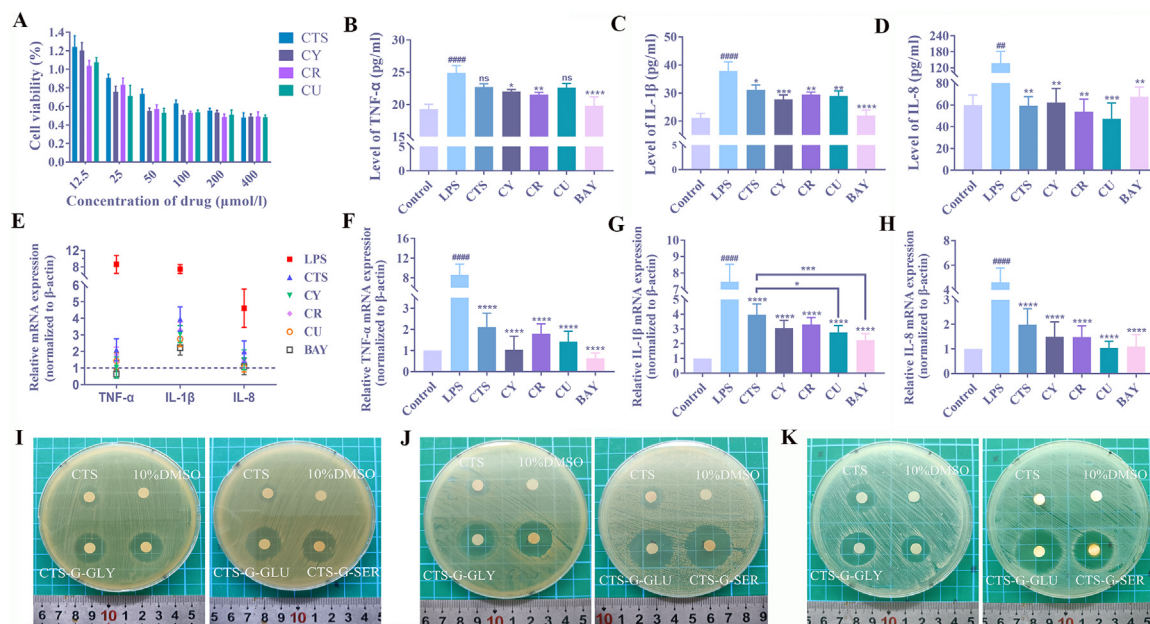
Fig. 5 – (A) The cell viability of HaCaT cells following incubation with formulations at different concentrations, $n = 5$. Expression levels of (B) TNF-α, (C) IL-1β, and (D) IL-8 in HaCaT cells under different treatment conditions (*$P < 0.05$, **$P < 0.01$, ***$P < 0.001$, ****$P < 0.0001$ vs. LPS, ##$P < 0.01$, ####$P < 0.0001$ vs. control, $n = 3$). (E) The impact of different formulations on the mRNA expression of inflammatory factors in HaCaT cells. Expression levels of (F) TNF-α mRNA, (G) IL-1β mRNA, and (H) IL-8 mRNA in HaCaT cells among various treatment groups (*$P < 0.05$, **$P < 0.01$, ***$P < 0.001$, ****$P < 0.0001$ vs. LPS, ####$P < 0.0001$ vs. control, $n = 3$). The inhibition zones of different formulations against (I) P. acnes, (J) Sau., and (K) Sep.

($P < 0.0001$ vs LPS), there was a significant downregulation observed. The effects were consistently comparable among the treatment groups, with the exception of the CU group and the positive control, which demonstrated lower levels of IL-1β mRNA expression in comparison to the CTS group ($P < 0.0001$, $P < 0.0001$ vs CTS). Finally, IL-8 mRNA expression also experienced significant upregulation as a result of LPS treatment ($P < 0.0001$ vs control). Post-treatment with CU and BAY11-7085, mRNA expression levels were restored to normal baseline levels (Fig. 5H), whereas the other groups exhibited variable degrees of downregulation.

The findings from RT-PCR offer additional support to the results presented in this section. They indicate that both CTS and self-assembled NPs achieve the downregulation of TNF-α, IL-1β, and IL-8 by modulating the MAPK/NF-κB signaling pathway, consequently manifesting their anti-inflammatory effects. Moreover, it was observed that in the context of reducing the expression of inflammatory factors, self-assembled NPs, on the whole, outperformed pure CTS, although statistical significance was only detected in a few instances. We remain of the opinion that the notably high cellular uptake efficiency of nanoparticles to some extent enhances the drug's efficacy (Fig. 4).

3.7. In vitro antibacterial efficiency of different formulations

In this study, *in vitro* antibacterial experiments were conducted to evaluate the antimicrobial activity of self-assembled NPs. The MIC results are presented in Table S6,

indicating that CTS exhibits inhibitory effects on Sep. and Sau. at concentrations of 0.125 µmol/ml or higher, and it demonstrates inhibitory effects on P. acnes at concentrations of 0.250 µmol/ml or higher. The self-assembled NPs, in comparison, displayed lower MIC values than CTS, indicating higher antibacterial efficiency. Notably, CU NPs exhibited over a fourfold increase in antibacterial efficiency compared to CTS against each microorganism. Additionally, agar diffusion assays confirmed the strong antibacterial activity of self-assembled NPs. Specifically, the order of inhibition zones against P. acnes was as follows: CU > CR > CY > CTS (Fig. 5I). For Sau., the order of inhibition zones was CR > CU > CY > CTS (Fig. 5J), while for Sep., the inhibition efficiency was ranked as CU > CR > CY > CTS (Fig. 5K). Detailed data on the diameters of the inhibition zones can be found in Table S7.

The above results unequivocally demonstrate that self-assembled NPs consistently manifest a more potent inhibitory effect on various acne-associated bacteria when compared to CTS. This phenomenon can be largely attributed to the presence of free amino groups at the hydrophilic terminus of CTS-peptide conjugates. These amino groups, through their capacity to attract H^+ ions from the surrounding solution and bear a positive charge, facilitate a mechanism akin to AMPs, allowing them to target the lipid bilayers of bacterial cell membranes. This targeting results in membrane permeation and eventual disruption of bacterial cell structures [28]. The antimicrobial effectiveness is intricately linked to the length of the peptide chain and the quantity of positive charges carried. Longer peptide chains with an increased positive charge exhibit more robust antibacterial effects.

Consequently, it is not surprising that CU demonstrates the most potent antibacterial effects among all the formulations in the majority of cases. This is because CU possesses the longest peptide chain segment, and its self-assembled supramolecular assemblies on the surface carry a substantial number of positive charges (Fig. 1E). To sum up, as an antimicrobial agent superior to CTS, CU holds great promise for application in antimicrobial therapy.

3.8. Animal experiments

3.8.1. Different formulations promote acne recovery in nude mice

To evaluate the potential *in vivo* application of self-assembled NPs, a fundamental pharmacological study was conducted at the animal level. CU was selected as the representative self-assembled NPs, considering its advantages in terms of self-assembly capability and antibacterial activity. Regarding the disease model, BALB/c-nu nude mice were chosen, and they were induced with *P. acnes* skin infections to establish the acne model, as per the research objectives [4]. This choice primarily stems from the fact that nude mice are immunocompromised animals without a thymus, rendering them more susceptible to *P. acnes* colonization and typically having an extended self-healing period. Additionally, nude mice exhibit degenerated and occluded hair follicles, along with a uniform distribution of sebaceous glands, providing an ideal environment for *P. acnes* colonization.

The *in vivo* experimental outcomes, depicted in Fig. 6A, illustrated that, on Day 1, all animals displayed localized skin swelling and inflammation on their backs, confirming the successful establishment of the acne model through intradermal injection of *P. acnes*. After 7 d of treatment, animals in different treatment groups showed varying degrees of recovery from acne-related swelling, while the control group (without treatment) displayed no significant improvement in skin swelling. In comparison to the control group, animals in the CTS group exhibited substantial improvement in skin swelling within 7 d, albeit some skin protrusion was still observed. In contrast, animals in the CU group had almost completely resolved skin cysts on Day 7, with the skin of the majority closely resembling that of control group. To facilitate a more direct comparison of acne swelling recovery among the animal groups, the swelling volume at the acne site was calculated for each animal. The line chart (Fig. 6B) depicts the trend in acne swelling volume changes. On Day 7 of treatment, the CTS and CU groups displayed a reduction in swelling volume by 64.9 % and 71.2 %, respectively ($P < 0.001$, $P < 0.0001$, *vs* control).

Following 7 d of treatment, skin tissues were collected, and the remaining quantity of *P. acnes* in the skin was quantified using the plate colony counting method (Fig. 6C). The *in vivo* antibacterial efficacy of each formulation was assessed as the ratio of *P. acnes* quantity in the treatment group to that in the control group (Fig. 6D). As anticipated, both CU and CTS significantly reduced the quantity of *P. acnes* in the skin ($P < 0.001$), with CU demonstrating superior antibacterial efficiency compared to CTS ($P < 0.05$). Furthermore, during the 7-d treatment period, no significant weight loss or skin

dryness and erythema were observed in the nude mice (Fig. 6E).

Upon analyzing the histological results (Fig. 6F), in comparison to the normal skin of nude mice (Blank), the control group of nude mice afflicted with acne cysts exhibited a substantial accumulation of pus within the cysts, primarily due to *P. acnes* infection. This accumulation imposed pressure on the surrounding tissues, resulting in a significant disruption of the skin structure. Moreover, there was a pronounced overall thickening of the skin, excessive keratinization of both the epidermis and hair follicles, visible dermal bleeding (red arrows), and conspicuous infiltration of inflammatory cells. Following treatment with CTS, there was a reduction in skin thickness, accompanied by a decrease in keratinization. However, some areas still displayed indications of inflammation infiltration and bleeding, and the overall skin structure remained somewhat disordered. In contrast, the CU group exhibited a substantial reduction in skin inflammation and keratinization. The skin structure appeared more organized, with a greater distribution of hair follicles in the dermal layer. The skin thickness closely resembled that of normal nude mice skin (Blank).

The results of *in vivo* evaluation highlighted the superior effectiveness of CU NPs hydrogel in reducing skin swelling and diminishing *P. acnes* presence within the skin compared to regular CTS hydrogel.

3.8.2. Effects of different formulations on expression of inflammatory pathway proteins

The inflammatory response of acne involves the activation of the NF-κB pathway. For example, *P. acnes* enters cells through pathways such as TLR2 and TLR4, triggering NF-κB-mediated inflammatory responses, leading to the release of cytokines such as TNF-α, IL-1β, IL-8, IL-6, activation of complement, and inflammasome formation, particularly those containing NLRP3 domains [45-47]. Previous studies have shown that CTS primarily inhibits the inflammatory response by downregulating the MAPK/NF-κB signaling pathway, inhibiting I-κB phosphorylation and NF-κB activation. Cell experiments in this study have also confirmed that self-assembled NPs similarly inhibit inflammation by downregulating this signaling pathway. Consequently, at the animal level, we embarked on immunohistochemistry to visually appraise the expression and spatial distribution of NF-κB and MAPK within the skin. This endeavor sought to evaluate how each formulation influenced inflammatory responses incited by acne.

The outcomes, as depicted in Fig. 7, conspicuously illustrate that animals in the blank group exhibit minimal expression of NF-κB (p65) and MAPK proteins (black arrows) within their skin. In stark contrast, the control group's skin prominently showcases elevated expression levels of NF-κB (p65) and MAPK proteins (brown areas). This serves as compelling confirmation of the successful induction of skin inflammation by *P. acnes*. Subsequent treatment with both CTS and CU manifestly engenders a reduction in the expression levels of NF-κB (p65) and MAPK within the skin. Relative quantitative results, as illustrated in Fig. S15A, indicate that CU significantly decreased the expression levels of NF-κB p65 in the skin of nude mice compared to the
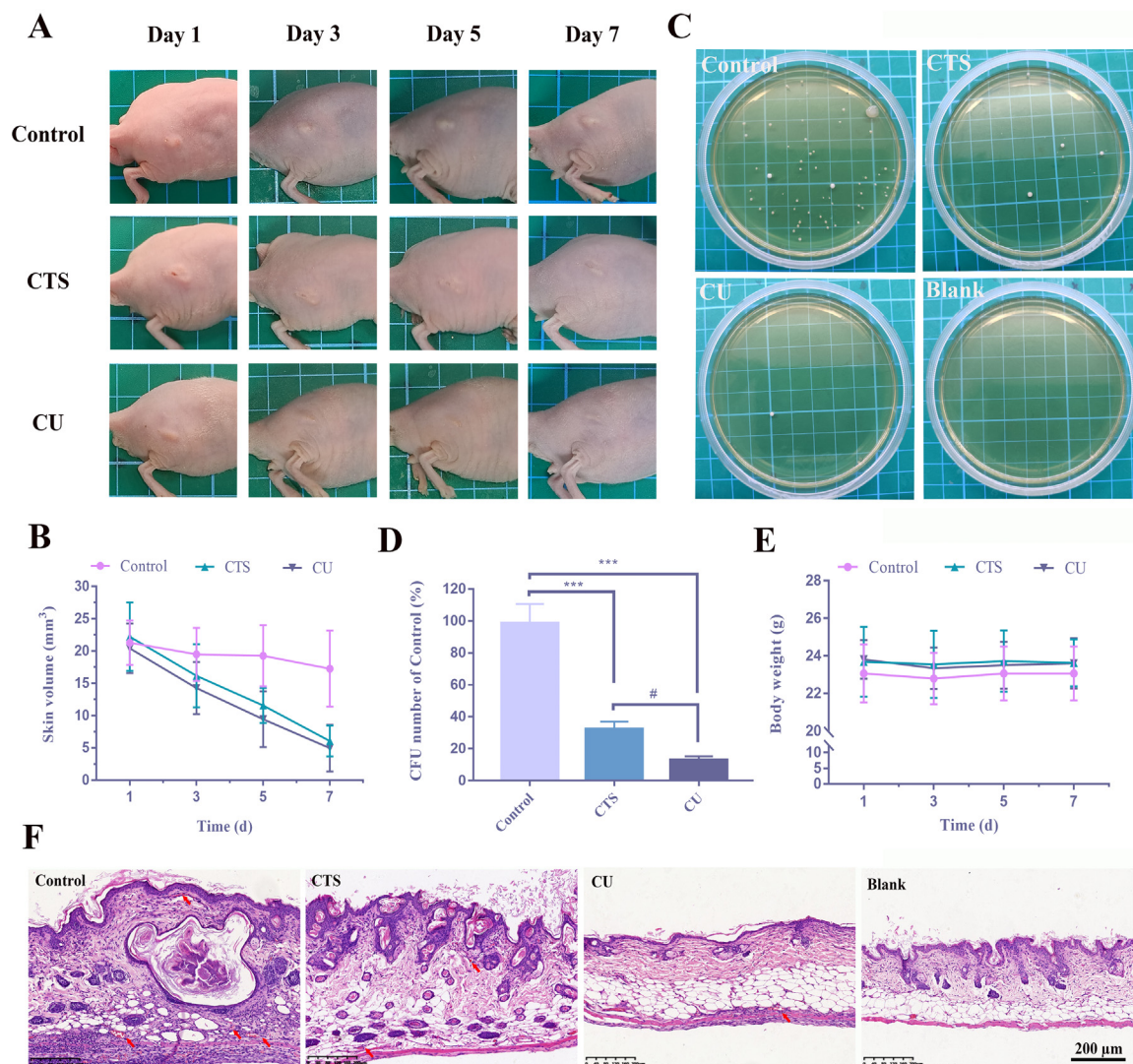
Fig. 6 – (A) Representative images of dorsal skin swelling in mice after 1, 3, 5 and 7 d of topical treatment with different formulations, $n = 6$. (B) The skin swelling volume of mice in each treatment group on Days 1, 3, 5 and 7, $n = 6$. (C) Plate culture images of *P. acnes* from the skin of mice in each group and (D) their relative quantities after 7 d of treatment ($n = 3$). (E) Changes in mouse body weight during the 7-d treatment period. (F) Representative images of HE staining of nude mouse skin with the scale bar set at 200 μm.
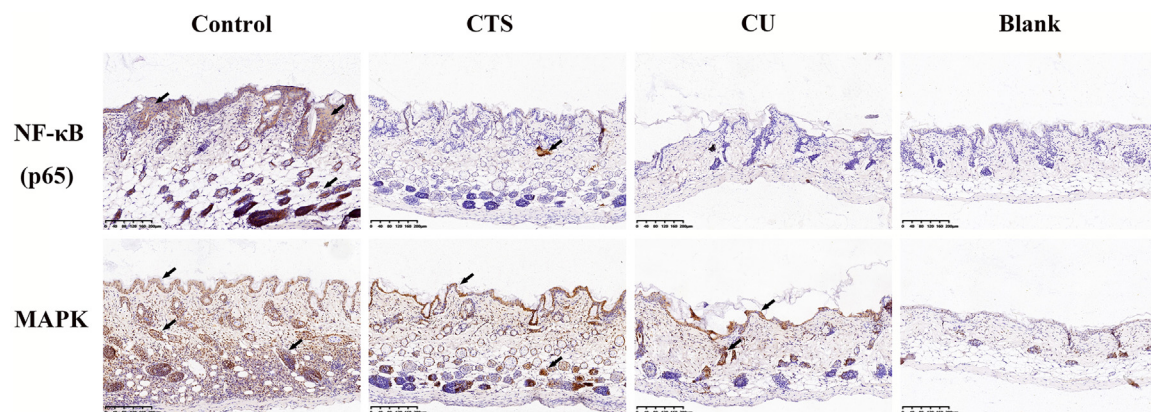

Fig. 7 – Immunohistochemistry slice images. Distribution of NF-κB (p65) and MAPK proteins in the skin of nude mice from various treatment groups, with the scale bar set at 200 μm.

control group ($P < 0.01$), with levels approaching those of the blank group. Conversely, the CTS group showed a slight reduction in NF-κB p65 expression, but this difference was not statistically significant ($P > 0.05$). Regarding MAPK (Fig. S15B), both formulations resulted in a reduction in its expression to varying extents ($P < 0.05$, $P < 0.001$), with a significant difference observed between the CU and CTS groups ($P < 0.05$).

These immunohistochemistry findings further substantiate the conclusions drawn from the cellular experiments, underlining that both CTS and CU bestow anti-inflammatory effects by modulating the MAPK/NF-κB signaling pathway. Notably, the *in vivo* application of CU proves to be more effective than CTS in mitigating acne-induced inflammatory responses.

4. Conclusions

This study focused on synthesizing CTS-peptide conjugates through acetylation at the C-1 position of CTS, followed by amide condensation reactions. Three CTS derivatives, namely CY, CR and CU, were obtained, and their chemical structures were elucidated using analytical techniques including ^{1}H NMR, HRMS, and FTIR. These derivatives exhibited varying degrees of increased solubility in aqueous solutions and reduced oil-water partition coefficients, thereby enhancing their skin penetrability. More importantly, the three derivatives can spontaneously assemble spherical supramolecular structures in aqueous environments and successfully construct carrier-free pure drug self-assembled nanosystems, that is, self-assembled NPs. To understand the assembly mechanism of these self-assembled NPs, MD simulations were employed. The results revealed that the assembly of CY, CR and CU primarily hinges on three non-covalent interactions, including hydrogen bonding, hydrophobic interactions, and π-π stacking. The spherical morphology of CY, CR and CU NPs can be attributed to robust hydrophobic interactions and π-π stacking, leading to a mutually perpendicular arrangement of molecules. This disrupts the hydrogen bond-driven coplanar structure and longitudinal growth trends. *In vitro* degradation experiments confirmed the esterase sensitivity of self-assembled NPs, resulting in expedited elimination from the body.

In terms of bioavailability, self-assembled NPs exhibited accelerated accumulation in mouse skin and efficient internalization into HaCaT cells, thereby facilitating their pharmacological effects. Concerning pharmacodynamics, the presence of positive charges and the structural characteristics of the peptide chains were found to enhance the antibacterial activity of self-assembled NPs, with CU NPs demonstrating notable efficacy. In the context of inflammation, both CTS and self-assembled NPs displayed anti-inflammatory effects by suppressing the MAPK/NF-κB pathway, consequently reducing the expression levels of inflammatory cytokines, including TNF-α, IL-1β and IL-8. This dual action of antibacterial and anti-inflammatory effects, combined with high bioavailability, rendered self-assembled NPs (CU) more effective in acne recovery compared to CTS.

In conclusion, the development of self-assembled NPs based on CTS-peptide conjugates presents a promising reference for CTS modification and the strategy of Carrier-free pure drug self-assembled nanosystems. This approach offers a novel avenue for clinical acne treatment. Nonetheless, it's imperative to underscore that further research is essential to assess the efficacy and safety of self-assembled NPs across various animal models, including humans, before potential future applications.

Conflicts of interest

The authors declare no competing financial interest.

Supplementary materials

Supplementary material associated with this article can be found, in the online version, at doi:10.1016/j.ajps.2024.100946.

REFERENCES

[1] Williams HC, Dellavalle RP, Garner S. Acne vulgaris. Lancet 2012;379(9813):361–72.

[2] Gollnick HP, Finlay AY, Shear NGlobal Alliance to Improve Outcomes in A. Can we define acne as a chronic disease? If so, how and when? Am J Clin Dermatol 2008;9(5):279–84.

[3] Jain A, Basal E. Inhibition of propionibacterium acnes-induced mediators of inflammation by Indian herbs. Phytomedicine 2003;10(1):34–8.

[4] Jeong S, Lee J, Im BN, Park H, Na K. Combined photodynamic and antibiotic therapy for skin disorder via lipase-sensitive liposomes with enhanced antimicrobial performance. Biomaterials 2017;141:243–50.

[5] Wang Z, Liu L, Xiang S, Jiang C, Wu W, Ruan S, et al. Formulation and characterization of a 3D-printed cryptotanshinone-loaded niosomal hydrogel for topical therapy of acne. AAPS PharmSciTech 2020;21(5):159.

[6] Arora MK, Yadav A, Saini V. Role of hormones in acne vulgaris. Clin Biochem 2011;44(13):1035–40.

[7] Patil V, Bandivadekar A, Debjani D. Inhibition of propionibacterium acnes lipase by extracts of Indian medicinal plants. Int J Cosmet Sci 2012;34(3):234–9.

[8] Guo C, Khengar RH, Sun M, Wang Z, Fan A, Zhao Y. Acid-responsive polymeric nanocarriers for topical adapalene delivery. Pharm Res 2014;31(11):3051–9.

[9] Simonart T. Newer approaches to the treatment of acne vulgaris. Am J Clin Dermatol 2012;13(6):357–64.

[10] Yu Z, Lv H, Han G, Ma K. Ethosomes loaded with cryptotanshinone for acne treatment through topical gel formulation. PLoS One 2016;11(7):e0159967.

[11] Kocak Z, Hatipoglu CA, Ertem G, Kinikli S, Tufan A, Irmak H, et al. Trimethoprim-sulfamethoxazole induced rash and fatal hematologic disorders. J Infect 2006;52(2):e49–52.

[12] Shree D, Patra CN, Sahoo BM. Novel herbal nanocarriers for treatment of dermatological disorders. Pharm Nanotechnol 2022;10(4):246–56.

[13] Azimi H, Fallah-Tafti M, Khakshur AA, Abdollahi M. A review of phytotherapy of acne vulgaris: perspective of new pharmacological treatments. Fitoterapia 2012;83(8):1306–17.

[14] Jiang Z, Gao W, Huang L. Tanshinones, critical pharmacological components in salvia miltiorrhiza. Front Pharmacol 2019;10:202.

[15] Sadeghi Z, Cerulli A, Marzocco S, Moridi Farimani M, Masullo M, Piacente S. Anti-inflammatory activity of tanshinone-related diterpenes from Perovskia artemisioides roots. J Nat Prod 2023;86(4):812–21.

[16] Zhu Z, Zeng Q, Wang Z, Xue Y, Chen T, Hu Y, et al. Skin microbiome reconstruction and lipid metabolism profile alteration reveal the treatment mechanism of cryptotanshinone in the acne rat. Phytomedicine 2022;101:154101.

[17] Chen BC, Ding ZS, Dai JS, Chen NP, Gong XW, Ma LF, et al. New insights into the antibacterial mechanism of cryptotanshinone, a representative diterpenoid quinone from salvia miltiorrhiza bunge. Front Terr Microbiol 2021;12:647289.

[18] Zuo T, Chen H, Xiang S, Hong J, Cao S, Weng L, et al. Cryptotanshinone-loaded cerasomes formulation: in vitro drug release, in vivo pharmacokinetics, and in vivo efficacy for topical therapy of acne. ACS Omega 2016;1(6):1326–35.

[19] Hou M, Gao YE, Shi X, Bai S, Ma X, Li B, et al. Methotrexate-based amphiphilic prodrug nanoaggregates for co-administration of multiple therapeutics and synergistic cancer therapy. Acta Biomater 2018;77:228–39.

[20] Wang Y, Cheetham AG, Angacian G, Su H, Xie L, Cui H. Peptide-drug conjugates as effective prodrug strategies for targeted delivery. Adv Drug Delivery Rev 2017;110-111:112–26.

[21] Karaosmanoglu S, Zhou M, Shi B, Zhang X, Williams GR, Chen X. Carrier-free nanodrugs for safe and effective cancer treatment. J Controlled Release 2021;329:805–32.

[22] Beaumont K, Webster R, Gardner I, Dack K. Design of ester prodrugs to enhance oral absorption of poorly permeable compounds: challenges to the discovery scientist. Curr Drug Metab 2003;4(6):461–85.

[23] Stella VJ, Nti-Addae KW. Prodrug strategies to overcome poor water solubility. Adv Drug Delivery Rev 2007;59(7):677–94.

[24] Simplicio AL, Clancy JM, Gilmer JF. Prodrugs for amines. Molecules 2008;13(3):519–47.

[25] Lopez-Abarrategui C, Alba A, Silva ON, Reyes-Acosta O, Vasconcelos IM, Oliveira JT, et al. Functional characterization of a synthetic hydrophilic antifungal peptide derived from the marine snail cenchritis muricatus. Biochimie 2012;94(4):968–74.

[26] Thapa RK, Diep DB, Tonnesen HH. Topical antimicrobial peptide formulations for wound healing: current developments and future prospects. Acta Biomater 2020;103:52–67.

[27] Nair SS, Zolotarskaya OY, Beckwith MJ, Ohman DE, Wynne KJ. A polycation antimicrobial peptide mimic without resistance buildup against propionibacterium acnes. Macromol Biosci 2017;17(9).

[28] Wimley WC. Describing the mechanism of antimicrobial peptide action with the interfacial activity model. ACS Chem Biol 2010;5(10):905–17.

[29] Liu K, Kang Y, Ma G, Mohwald H, Yan X. Molecular and mesoscale mechanism for hierarchical self-assembly of dipeptide and porphyrin light-harvesting system. Phys Chem Chem Phys 2016;18(25):16738–47.

[30] Doerr F, George J, Schmitt A, Beleggia F, Rehkamper T, Hermann S, et al. Targeting a non-oncogene addiction to the ART/CHK1 axis for the treatment of small cell lung cancer. Sci Rep 2017;7(1):15511.

[31] Cheetham AG, Chakroun RW, Ma W, Cui H. Self-assembling prodrugs. Chem Soc Rev 2017;46(21):6638–63.

[32] Meng F, Zhou J, Cheng X, Xu J, Kang L, Li D, et al. Design, synthesis and cardioprotection of cryptotanshinone derivatives. Chinese J Org Chem 2022;42(6):1735–46.

[33] Nielsen JB, Nielsen F, SØRensen JA. In vitro percutaneous penetration of five pesticides—effects of molecular weight and solubility characteristics. Ann Occup Hyg 2004;48(8):697–705.

[34] Sloan KB, Koch SA, Siver KG, Flowers FP. Use of solubility parameters of drug and vehicle to predict flux through skin. J Invest Dermatol 1986;87(2):244–52.

[35] Abraham MH, Chadha HS, Mitchell RC. The factors that influence skin penetration of solutes. J Pharm Pharmacol 1995;47(1):8–16.

[36] Li SS, Song ZH, Xiong LQ, Zhang Q, Liu Q, Li GF. The percutaneous permeability and absorption of dexamethasone esters in diabetic rats: a preliminary study. Drug Deliv 2014;21(1):17–25.

[37] Hawkins GS, Reifenrath WG. Influence of skin source, penetration cell fluid, and partition coefficient on in vitro skin penetration. J Pharm Sci 1986;75(4):378–81.

[38] Bianco A, Kostarelos K, Prato M. Making carbon nanotubes biocompatible and biodegradable. Chem Commun 2011;47(37):10182–8.

[39] Guelcher SA, Srinivasan A, Dumas JE, Didier JE, McBride S, Hollinger JO. Synthesis, mechanical properties, biocompatibility, and biodegradation of polyurethane networks from lysine polyisocyanates. Biomaterials 2008;29(12):1762–75.

[40] Ahn S, Siddiqi MH, Aceituno VC, Simu SY, Zhang J, Jimenez Perez ZE, et al. Ginsenoside Rg5:Rk1 attenuates TNF-α/IFN-γ-induced production of thymus- and activation-regulated chemokine (TARC/CCL17) and LPS-induced NO production via downregulation of NF-κB/p38 MAPK/STAT1 signaling in human keratinocytes and macrophages. In Vitro Cell Dev-An 2016;52(3):287–97.

[41] He C, Hu Y, Yin L, Tang C, Yin C. Effects of particle size and surface charge on cellular uptake and biodistribution of polymeric nanoparticles. Biomaterials 2010;31(13):3657–66.

[42] Ho LWC, Liu Y, Han R, Bai Q, Choi CHJ. Nano-cell interactions of non-cationic bionanomaterials. Acc Chem Res 2019;52(6):1519–30.

[43] Li J, Zheng M, Wang C, Jiang J, Xu C, Li L, et al. Cryptotanshinone attenuates allergic airway inflammation through negative regulation of NF-κB and p38 MAPK. Biosci Biotechnol Biochem 2020;84(2):268–78.

[44] Nagy I, Pivarcsi A, Kis K, Koreck A, Bodai L, McDowell A, et al. Propionibacterium acnes and lipopolysaccharide induce the expression of antimicrobial peptides and proinflammatory cytokines/chemokines in human sebocytes. Microbes Infect 2006;8(8):2195–205.

[45] Xu H, Li H. Acne, the skin microbiome, and antibiotic treatment. Am J Clin Dermatol 2019;20(3):335–44.

[46] Kanwar IL, Haider T, Kumari A, Dubey S, Jain P, Soni V. Models for acne: a comprehensive study. Drug Discoveries Ther 2018;12(6):329–40.

[47] Ghasemiyeh P, Mohammadi-Samani S, Noorizadeh K, Zadmehr O, Rasekh S, Mohammadi-Samani S, et al. Novel topical drug delivery systems in acne management: molecular mechanisms and role of targeted delivery systems for better therapeutic outcomes. J Drug Delivery Sci Technol 2022;74:103595.